Supplementary Material

Deep co-deposition of polydopamine in PVDF hydrogel to enhance photothermal evaporation efficiency

Yu Ma,*[a,b] Lan Yang,[a] Shangdi Wu,[a] Liran Xu[a] and Hua Huang*[a]

[a] China Coal Technology & Engineering Group Nanjing Design & Research Institute Co., Ltd, Nanjing, 210031, China

[b] Guangdong Key Laboratory of Integrated Agro-environmental Pollution Control and Management, Guangdong Institute of Eco-environmental Science & Technology, Guangzhou, 510650, China

* Corresponding author. Email: h.huang.ccteg@gmail.com; mayutech03@gmail.com.

Reaction mechanisms

The interaction between Fe and PDA was evidenced by the Fe 2p spectrum of PDA-Fe, which exhibited peaks at 711.4 and 724.2 eV, corresponding to Fe^{2+}-O(2p3/2) and Fe^{2+}-O(2p3/2) bindings, respectively. In contrast, the PDA-KH550-Fe spectrum revealed peaks at 713.8 and 730.3 eV, indicative of Fe^{3+}-O(2p3/2) and Fe^{3+}-O(2p3/2) bindings (**Figure S1a**). This suggests that during the reaction between PDA and Fe^{3+}, a significant portion of Fe^{3+} is reduced to Fe^{2+}, whereas KH550 acts as an oxidant, preserving Fe^{3+} from reduction[1]. Furthermore, the O1s spectrum of both PDA-KH550-Fe and PDA-gel3 membrane displayed a characteristic peak at approximately 530.40 eV, attributed to O−Fe binding, providing strong evidence for O−Fe coordination within the membranes (**Figure S1b**)[1]. The prominent N 1s peak observed at 399.8 eV corresponds to pyrrolic N, which constitutes the primary form of the N element in PDA, Fe-PDA, and PDA-gel3 (**Figure S1c**). In the carbon shift spectra (**Figure S1d**), one of the most prominent peaks was ascribed to C=C binding on the benzene ring[1]. Collectively, these spectra confirm that iron predominantly exists in PDA as Fe^{3+} and forms a stable coordination with phenolic hydroxyl oxygens on polydopamine.

Regarding the interaction between KH550 and PDA, the O1s spectrum of PDA-KH550, PDA-KH550-Fe, and PDA-gel3 membrane exhibited a characteristic peak at approximately 532.70 eV, indicating Si-O binding. This confirms the presence of KH550 in these materials (**Figure S1b**) [2]. In the N 1s spectrum of the PDA-gel3 membrane, the binding energy located at 400.0 eV corresponds to C-NH_2 groups on both KH550 and PDA molecules, suggesting the successful complexation of KH550 with PDA (**Figure S1c**)[3]. **Figure S1d** presents the high-resolution XPS C1s peak of PDA-KH550 and PDA-gel3, which can be deconvoluted into four core-level peaks: C-Si (283.6 eV), C-N/C-O (285.1 eV), and C=O (288.2 eV), respectively [4-6]. The C-N species originate from dopamine or KH550, while the C-Si peak is attributed to KH550. This confirms the successful chemical reaction between KH550 and dopamine.

In summary, KH550 can undergo chemical reactions with PDA, enhancing the adhesion between dopamine. Additionally, PDA reacts with ferric ions, reducing them to ferrous ions. The oxidizing property of KH550 allows the Fe ions in the reaction system to remain in the ferric state, enabling them to chelate with more polydopamine.

This imparts stronger electron-withdrawing properties to the iron ions, allowing them to act as electron acceptors and interact with catechol groups, thereby generating multiple donor-acceptor pairs within the Fe-PDA system.

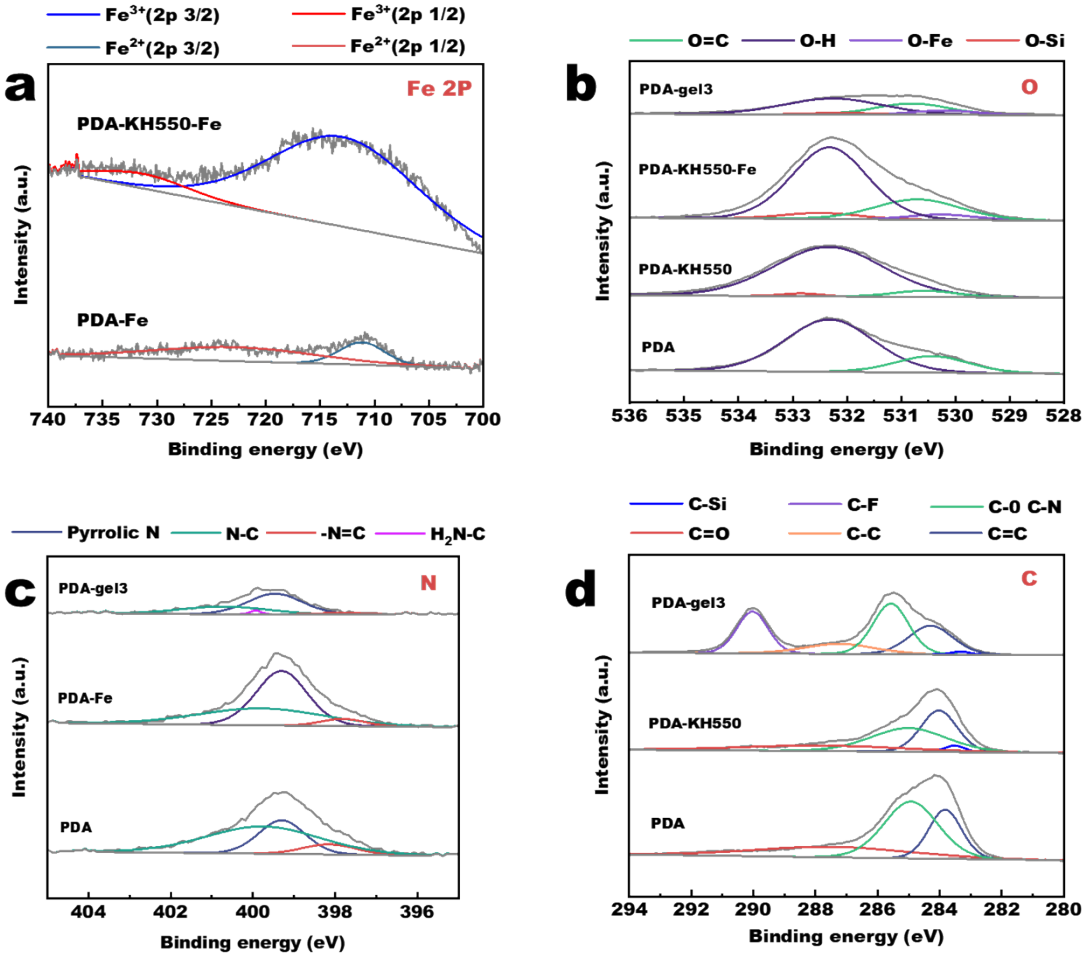

Figure S1. X-ray photoelectron spectroscopy (XPS) scans of PDA, PDA-KH550, PDA-Fe+, PDA-KH550-Fe+, and PDA-gel3, O 1s, N 1s, C 1s, and Fe 2p, shifts, and an XPS survey spectrum.

Mechanical properties

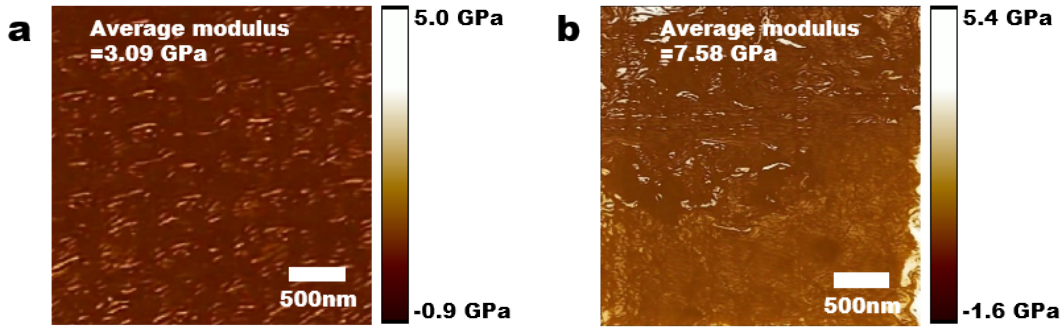

Figure S2. (a) DMT modulus of a PVDF-H membrane, (b) DMT modulus of a commercial PVDF membrane (d) (PF-QNM mode, AFM).

Membrane structure

The pore sizes and porosities of the membranes were measured utilizing a high-performance automatic mercury injection instrument (Micromeritics Instrument Corporation, AutoPore LV 9510). As illustrated in **Figure S3**, the pore size distribution of the PDA-gelX membranes remains largely consistent. Notably, with the exception of the PDA-gel1 membrane, which exhibits a relatively larger average pore size of 325.8 nm, the average pore sizes of the other PDA-gel membranes remain relatively unchanged, hovering around 200 nm. Remarkably, a significant alteration is observed in the porosity of the PDA-gelX membranes (**Figure S3b**). As 'X' increases, the porosity decreases substantially, ranging from 80.95% for PDA-gel1 down to 28.09% for PDA-gel8. These findings suggest that the denser membrane structure observed in **Figure 4e, h, k, n** is primarily attributed to the reduction in porosity, rather than a decrease in average pore size.

For porous water treatment separation membranes, the relationship between membrane flux and membrane structure can be expressed through the Hagen–Poiseuille equation[7]:

$$J_v = \frac{\epsilon \pi r_p^2 \Delta P}{8 \mu L} \tag{S1}$$

Where J_v is the flux; r_p is the average pore radius of membrane; ϵ is the porosity; ΔP is the transmembrane pressure; and μ is the water viscosity; L is the membrane thickness. It can be observed that the membrane flux is related to the membrane thickness, pore size within the membrane, and porosity of the membrane structure. However, the transmembrane pressure difference ΔP, which is essential for calculating the membrane flux, remains unknown.

In this study, the photothermal evaporation process involves the partial evaporation of the liquid within the membrane pores, leading to the continuous formation of gas-liquid interfaces. This results in a positive Laplace force that drives the replenishment of water to the membrane surface. The Laplace force generated within the membrane pores can be simply described by the Young-Laplace equation:

$$\Delta P = \frac{2\delta}{r_c} \tag{S2}$$

in which, δ represents the surface tension of water, and r_c is the radius of curvature of the concave meniscus within an ideal cylindrical membrane pore channel. Here, we approximate r_c to be approximately equal to the average radius of the membrane pores, r_p. Therefore, the Laplace force generated within the membrane can be considered as the transmembrane pressure difference. Consequently, by combining **Eq. S1** and **Eq. S2**, it can be inferred that:

$$J_v \approx \frac{\epsilon \pi \delta r_p}{4\mu L} \tag{S3}$$

It can be observed that the water transport rate within the membrane in this study is positively correlated with the porosity and pore size and negatively correlated with the thickness. By consulting a table of water viscosity and surface tension as functions of temperature, and combining the porosity data from **Figure S3b** with the membrane thickness data from **Figure 4f, i, l, o**, the flux of the PDA-gelX membranes can be approximately calculated as: 4.07×10^{-5} m·s^{-1} for PDA-gel1, 1.48×10^{-5} m·s^{-1} for PDA-gel3, 2.95×10^{-6} m·s^{-1} for PDA-gel5, and 8.57×10^{-7} m·s^{-1} for PDA-gel8. Notably, the flux of the PDA-gel8 membrane is an order of magnitude lower than that of the PDA-gel3 membrane. Consequently, the excessively low flux of the PDA-gel8 membrane during the photothermal evaporation process prevents the timely replenishment of water lost due to evaporation, thereby reducing the evaporation rate. In terms of light absorption, **Figure 5c** indicates that as 'X' increases, there is no significant enhancement in light absorption. This phenomenon suggests that changes in the membrane surface structure have a relatively minor impact on its light absorption capability, indicating that specific light-trapping structures did not form on the membrane surface.

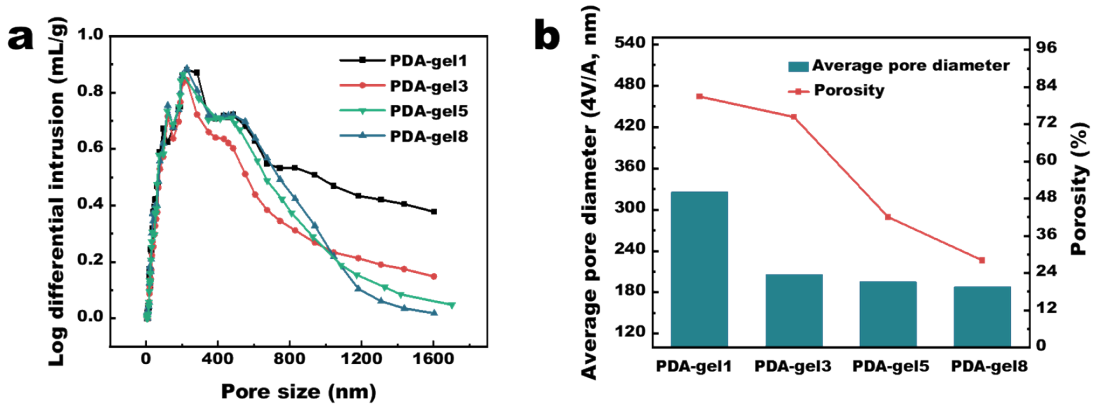

Figure S3. Pore size distribution(a) and average pore diameter and porosity (b) of the PDA-gel1, PDA-gel3, PDA-gel5 and PDA-gel8.

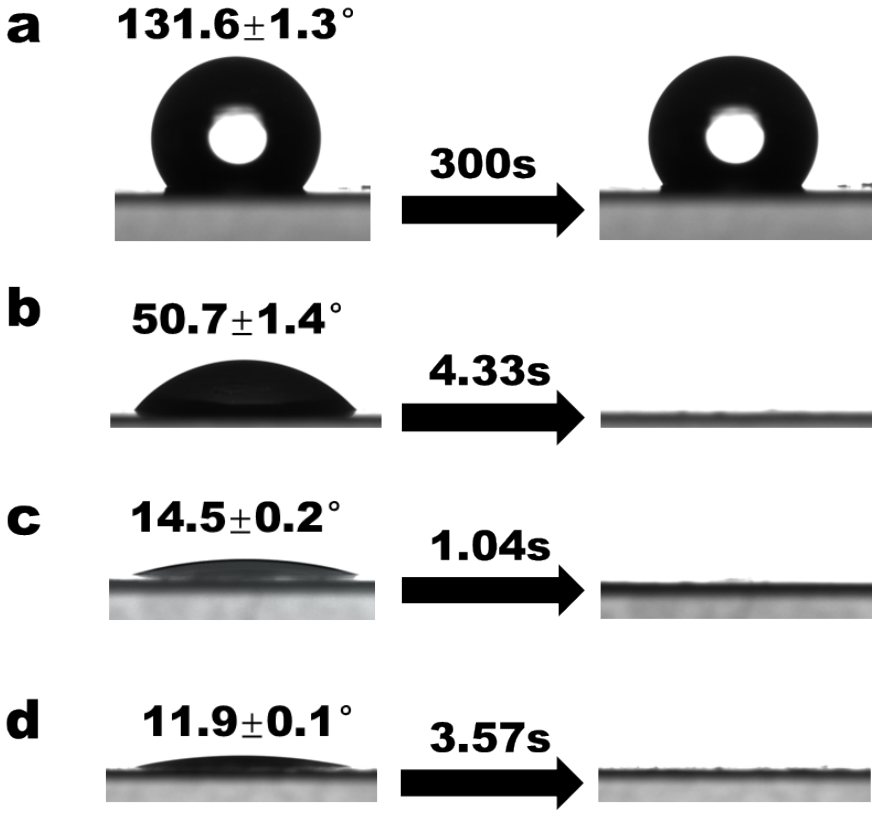

Figure S4. Water contact angles of the commercial PVDF membrane (a), PVDF-C membrane (b), PDA-gel3 membrane, and PDA-gel8 membrane.

Photothermal properties

The photothermal conversion efficiency of both the deep co-deposition (PDA-gel3) and the conventional surface co-deposition method (PVDF-C) membranes were computed utilizing the approach proposed by Wu et al. [8].

The external photothermal efficiency of the membranes, denoted as η_{ext}, is determined by the equation below:

$$\eta_{ext} = \frac{Q}{q} \quad \text{（S4）}$$

where Q is thermal energy raised from irradiation and q is nominal of direct solar irradiation on the material.

Under ambient conditions, when exposed to a specified solar irradiation, the membrane absorbs solar light, converts it into heat, and subsequently dissipates this energy by transferring it to the surrounding air. The energy balance for this system can be represented by the following equation:

$$Q - Q_{sur} = c \times m \times \frac{dT}{dt} \quad \text{（S5）}$$

in which Q is the heat generated, Q_{sur} is the heat dissipated, c and m are heat capacity and mass of the membrane, respectively, T is the surface temperature of the membrane, and t is time.

When subjected to a specific solar irradiation power, the temperature of the membranes initially increases and ultimately reaches a maximum temperature, T_{max}, at which point the energy input and output are in equilibrium, as follows:

$$Q = Q_{sur}^{max} = h \times s \times \left(T_{max} - T_{sur}^{max}\right) \quad \text{（S6）}$$

in which h refers to a heat transfer coefficient, s is the surface area of the membrane for heat dissipation, and T_{sur}^{max} is the temperature of the surrounding environment temperature of surrounding to its maximum equilibrium temperature.

The rate constant of the energy loss w can be written as:

$$w = \frac{h \times s}{c \times m} \quad \text{（S7）}$$

Ultimately, the relationship between temperature and time can be expressed in

the following form:

$$T(t) = A \times \exp(-w \times t) + B \times \exp\left(-w_{sur} \times t\right) + C \quad \text{(S8)}$$

In which, $A = T_{max} - B - C$, $B = \frac{w}{w - w_{sur}} \times \left(T_{sur}^{max} - T_{sur}^{0}\right)$, $and\ C = T_{sur}^{0}$

where w_{sur} is the rate constant of the energy transfer in the surrounding environment similar to *w*, and T_{sur}^{0} represents the stable room temperature under the investigation

Eq. S8 can be utilized to fit the experimental results. As depicted in **Figure 5g** and **Figure S5**, during the experiment, the membranes were initially freeze-dried and then cut into circles with a diameter of 3.5 cm. Subsequently, they were placed on a non-woven fabric (inset in **Figure S5a**) to test the change in membrane surface temperature over time under one solar illumination (1 kW·m^{-2}). Additionally, following the stabilization of both the ambient and membrane surface temperatures, the change in membrane surface temperature over time was monitored after the solar simulator was turned off (**Figure 5g**). As shown in **Figure S5**, the $T_{max} - T_{sur}^{max}$ of the PVDF-C and PDA-gel3 membranes were about 15.6℃ and 20.8℃, respectively. Additionally, by applying **Eq. S8** to fit the cooling data from the experiments, the $h \times s$ values for the PVDF-C and PDA-gel3 membranes were determined to be around 3.93 mW·°C^{-1} and 3.96 mW·°C^{-1}, as shown in **Figure 5g**. The mass of each sample, *m*, was measured, and the heat capacity, *c*, was taken as 1142 J/(kg·K) for the PVDF material. By substituting all the parameters into Eqs. S1-S5, the external photothermal conversion efficiencies, η_{ext}, for the PVDF-C and PDA-gel3 membranes were calculated to be approximately 73.47% and 87.93%, respectively. It is important to highlight that, as illustrated in **Table 1** and **Figure 5a**, 91.18% of the total solar energy was absorbed according to the reflectance measurements. This indicates that the quantum efficiencies, which represent the ratio of absorbed photons to generated heat[9, 10], were 80.58% and 96.43% for the PVDF-C and PDA-gel3 membranes, respectively. In other words, the photothermal conversion efficiency and quantum efficiency of the PDA-gel3 membrane exhibited significant improvement

compared to the PVDF-C membrane.

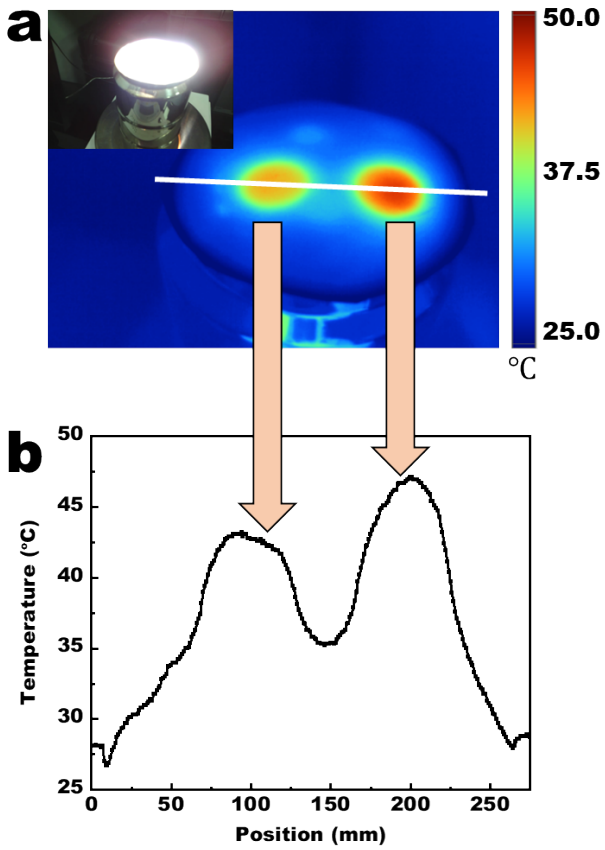

Figure S5. (a) IR image of the samples during the light on. Inset is the digital image of the samples during the light on (1 kW·m^{-2}); (b) The temperature relationship with position in Figure S5a after 600 s illumination under 1 sun.

Long-term stability

The long-term stability of the PDA-gel3 membrane under varying pH values, temperatures, and ion strengths have been tested. Specifically, to assess the long-term stability of the membrane across different pH levels, HCl solutions at 0.0001 mol/L (pH=4) and 1 mol/L (pH=0), as well as NaOH solutions at 0.0001 mol/L (pH=10) and 1 mol/L (pH=14) were prepared. As shown in **Figure S7a**, under weak acid and weak alkaline conditions, the PDA-gel3 membrane exhibits excellent long-term stability in terms of water evaporation rate when subjected to one solar illumination (1 $kW \cdot m^{-2}$) at 25℃. However, under strong acid and strong alkaline conditions (with all other conditions remaining the same), our tests revealed an obvious decrease in the water evaporation rate of the PDA-gel3 membrane. In particular, under strong alkaline conditions, the water evaporation rate of the membrane decreased to approximately 0.5 $kg \cdot m^{-2} \cdot h^{-1}$ within 24 hours and then stabilized, indicating that the membrane lacks long-term stability in strong alkaline solutions. As shown in **Figure S7b**, when the membrane was immersed in high-concentration NaOH and HCl solutions for 2 hours, we observed that the color of the NaOH solution gradually turned yellow, suggesting that the PDA loaded within the membrane dissolved in the strong alkaline solution. These results indicate that the PDA-gel3 membrane exhibits good long-term stability under normal pH conditions but cannot withstand the impact of strong acid or strong alkaline liquids, which is consistent with previously reported findings in the literature[11].

As shown in **Figure S7c**, the surface temperature and evaporation rate of the PDA-gel3 membrane remained stable during the test, indicating that the membrane exhibits good long-term stability at higher temperatures. Moreover, as depicted in **Figures S7d-e**, the material of the PDA-gel3 membrane begins to decompose at approximately 263.31℃ and is nearly fully decomposed by around 472.45℃. Notably, the material exhibits good thermal stability in normal environmental conditions (up to 200℃), as indicated in the insert of **Figure S7e**.

To test the long-term stability of the PDA-gel3 membrane under different ionic strengths, we prepared NaCl solutions with concentrations of 900 mg/L, 1500 mg/L, 3000 mg/L, 5000 mg/L, and 10000 mg/L. As shown in **Figure S7f**, the membrane exhibits good long-term stability at lower ionic strengths. When the ionic strength exceeds 5000 mg/L, the long-term water evaporation rate of the membrane decreases.

This may be due to the deposition of salt on the membrane surface and within the membrane [12].

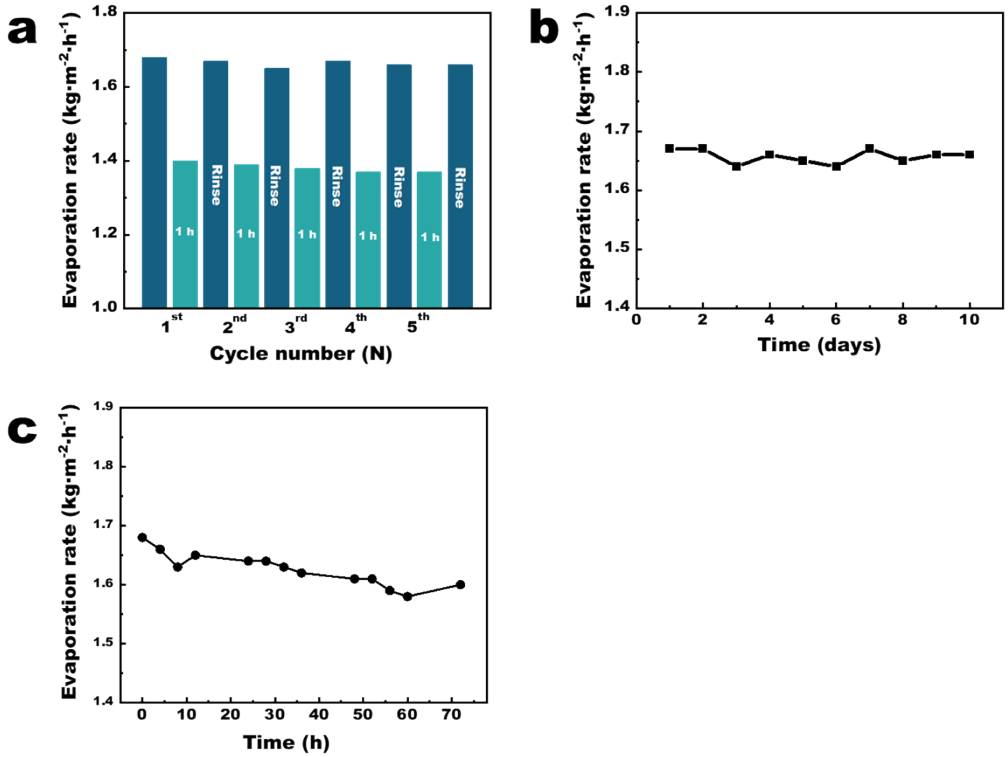

Figure S6. (a) Evaporation cycle performance of the PDA-gel3 membrane; (b) long-term stability of the PDA-gel3 membrane in pure water; (c) long-term stability of PDA-gel3 membrane in brine.

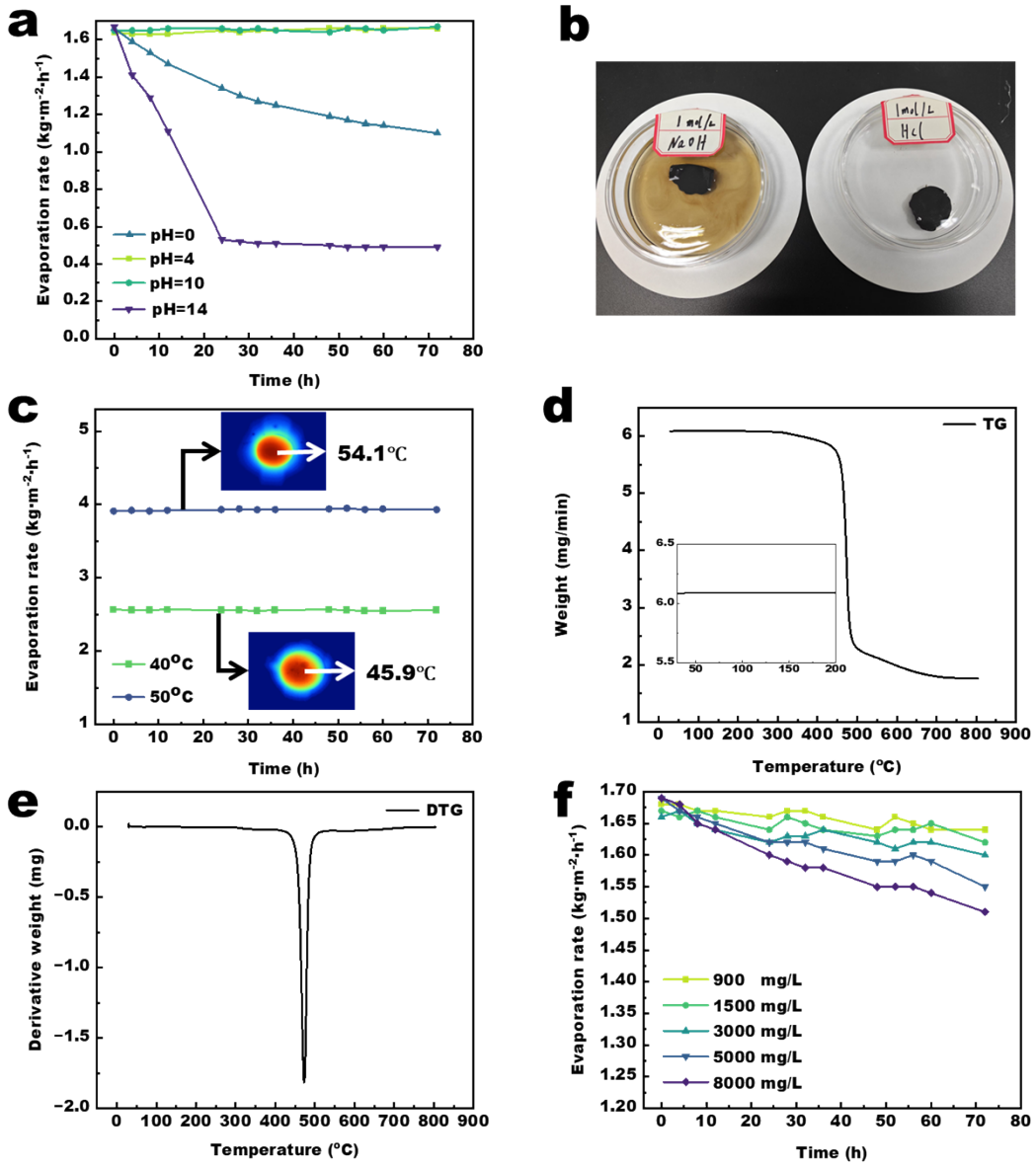

Figure S7. Long-term stability of the PDA-gel3 membrane under various environmental conditions. (a) Long-term evaluation of the evaporation rate of the PDA-gel3 membrane at different pH levels; (b) Digital image of the membranes immersed in 1 mol/L NaOH and 1 mol/L HCl solutions, respectively; (c) Long-term evaluation of the evaporation rate of the PDA-gel3 membrane at different temperatures, Insets: infrared images of the membrane at different temperatures; (d) Long-term assessment of the evaporation rate of the PDA-gel3 membrane under different ionic strength; (e) The TG curves of the PDA-gel3 membranes; (f) The DTG curves of the PDA-gel3 membranes.

References

1. N. Xu, A. Hu, X. M. Pu, J. F. Li, X. M. Wang, J. Wang, Z. B. Huang, X. M. Liao and G. F. Yin, *ACS Applied Materials & Interfaces*, 2022, **14**, 15894-15910.
2. Y. L. Khung, S. H. Ngalim, A. Scaccabarozzi and D. Narducci, *Beilstein Journal of Nanotechnology*, 2015, **6**, 19-26.
3. L. Z. Xu, Y. B. Chen, Y. Y. Zhang, M. Wang, S. Y. Wei and X. Y. Zhao, *Desalination*, 2024, **583**, 117718.
4. L. Zhou, Y. He, H. Shi, G. Q. Xiao, S. H. Wang, Z. Y. Li and J. Y. Chen, *Journal of Hazardous Materials*, 2019, **380**, 120865.
5. C. J. Wei, X. H. Zhang, S. Y. Ma, C. X. Zhang, Y. Li, D. J. Chen, H. Jiang, Z. K. Xu and X. J. Huang, *Chemical Engineering Journal*, 2021, **425**, 130118.
6. S. Li, X. Li, M. C. Shao, J. L. Yang, Q. H. Wang, T. M. Wang and X. R. Zhang, *Tribology International*, 2019, **140**, 105861.
7. S. Déon, A. Escoda and P. Fievet, *Chemical Engineering Science*, 2011, **66**, 2823-2832.
8. J. Wang, Y. Y. Li, L. Deng, N. N. Wei, Y. K. Weng, S. Dong, D. P. Qi, J. Qiu, X. D. Chen and T. Wu, *Advanced Materials*, 2017, **29**, 1603730.
9. M. M. Gao, L. L. Zhu, C. K. Peh and G. W. Ho, *Energy & Environmental Science*, 2019, **12**, 841-864.
10. X. H. Liu, D. D. Mishra, X. B. Wang, H. Y. Peng and C. Q. Hu, *Journal of Materials Chemistry A*, 2020, **8**, 17907-17937.
11. C. Zhang, Y. Ou, W. X. Lei, L. S. Wan, J. Ji and Z. K. Xu, *Angewandte Chemie-International Edition*, 2016, **55**, 3054-3057.
12. Y. D. Kuang, C. J. Chen, S. M. He, E. M. Hitz, Y. L. Wang, W. T. Gan, R. Y. Mi and L. B. Hu, *Advanced Materials*, 2019, **31**, 1900498.